

Variable L_0 Guidance Strategy: Enlarged Operational Envelope and Path-Following *

Amit Shivam, * Manuel C.R.M. Fernandes, *
Fernando A.C.C. Fontes, * Lorenzo Fagiano **

* Department of Electrical and Computer Engineering, Faculdade de Engenharia, Universidade do Porto, Porto, Portugal

(e-mail: amitshivam@alum.iisc.ac.in, {mcrmf, faf}@fe.up.pt).

** Department of Electronics, Information and Bioengineering, Polytechnic University of Milan, Italy

(e-mail: lorenzo.fagiano@polimi.it)

Abstract:

This paper presents a geometric and theoretical study of an exponentially varying look-ahead parameter for UAV path-following guidance. Conventional guidance laws with a fixed look-ahead distance often drive the vehicle into turn-rate saturation when the heading or cross-track error is large, leading to constrained maneuvers and higher control effort. The proposed variable L_0 strategy reshapes the look-ahead profile so that the guidance command adapts to the evolving tracking error geometry. A detailed investigation shows that this adaptation significantly enlarges the region in which the commanded turn rate remains unsaturated, allowing the vehicle to operate smoothly over a broader range of error conditions. For representative settings, the unsaturated operational envelope increases by more than 70% relative to the constant L_0 formulation. These geometric insights translate to smoother trajectories, earlier recovery from saturation, and reduced control demand. Simulation studies on straight-line and elliptical paths demonstrate the merits of the variable look-ahead strategy, highlighting its control-efficient and reliable path-following performance.

Keywords: Uncrewed Aerial Vehicles, Path-following, L_0 and L_1 guidance

1. INTRODUCTION

The rapid expansion of uncrewed aerial vehicles (UAVs) in security, environmental monitoring, medical logistics, and civilian automation has increased the need for reliable path-following guidance systems. These applications often require UAV to autonomously follow a desired geometric path while considering the vehicle's kinematic and actuator constraints. Although several guidance laws provide stable convergence, most rely on fixed look-ahead distances or curvature parameters that do not adapt when the vehicle experiences large heading deviations or significant lateral offsets. Under such conditions, the commanded turn rate often saturates, leading to constrained maneuvers and elevated control effort. This underscores the importance of guidance strategies with a large operational envelope, that is, the range of tracking errors for which the controller can operate without saturating the actuators. Expanding this envelope directly improves tracking smoothness, energy usage, and actuator-feasible behavior. However, despite progress in UAV guidance design, the underlying geomet-

ric structure of this operational envelope and the factors governing its boundary remains largely unexplored.

Several path-following strategies have been developed to address some of these issues. Waypoint-based navigation Osborne and Rysdyk (2005); Hota and Ghose (2014) and control-theoretic approaches such as MPC Alessandretti et al. (2013), LQR Lee et al. (2010), and sliding-mode control Kumar et al. (2024) provide systematic frameworks for trajectory tracking. Vector-field methods Frew et al. (2008); Pothen and Ratnoo (2017); Goncalves et al. (2009); Kapitanyuk et al. (2017); Nelson et al. (2007); Shivam and Ratnoo (2021, 2023) and virtual-target or L_1 -type guidance laws (L_1 is the distance between the vehicle and the virtual target on the desired path) Breivik and Fossen (2005); Park et al. (2004, 2007); Curry et al. (2013); Stastny (2018) remain popular due to their computational simplicity and robustness. Variable look-ahead formulations have been explored for straight-line Lekkas and Fossen (2012) and spline-based paths Lekkas and Fossen (2014), while trajectory-shaping guidance laws have been proposed for curved path following Ratnoo et al. (2015). In the later course of work, Thakar and Ratnoo (2017) developed lead-angle-based guidance logic, which further improves transient performance and settling times in comparison to Park et al. (2007); Ratnoo et al. (2015). The constant L_0 guidance framework introduced in Silva et al. (2019) enlarged the domain of attraction relative to

* This research has been supported by the Italian Ministry of Enterprises and Made in Italy under grant "4DDS - 4D Drone Swarms" and by FCT/MCTES (PID-DAC), through project 2022.02801.PTDC-UPWIND-ATOL (<https://doi.org/10.54499/2022.02801.PTDC>) and grant 2021.07346.BD.

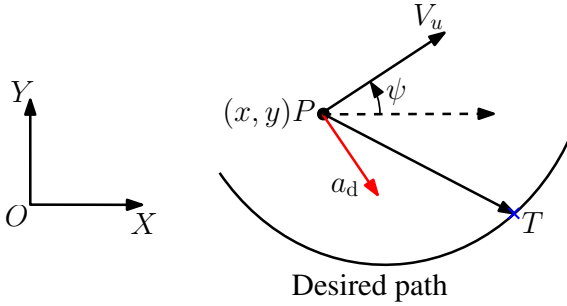


Fig. 1. Path-following geometry.

the classical L_1 setting and was later analyzed for curved paths Fernandes and Fontes (2024) when integrated with predictive control schemes Fernandes et al. (2020). Comparative studies such as Fernandes et al. (2022) further highlight the practical need for these variants.

Although these methods provide meaningful improvements, the existing literature offers limited theoretical insight into how the look-ahead parameter—whether fixed or adaptive—shapes the boundary between saturated and unsaturated operation. In particular, a clear geometric characterization of the operational envelope, and the factors that determine the onset of saturation, lacks in the literature.

Motivated by this gap, the present work offers a geometric and theoretical study of an exponentially varying L_0 profile and examines its impact on the path-following behavior of a UAV kinematic model. Building on preliminary observations reported in Fernandes et al. (2025), we show that the proposed variable L_0 formulation significantly enlarges the range of tracking conditions under which the guidance command remains unsaturated. This expanded operational envelope enables the controller to operate smoothly across a broader set of error scenarios, leading to earlier recovery from saturation, smoother trajectories, and reduced control effort. The geometric analysis provides explicit criteria that characterizes when saturation occurs and when it can be avoided. Simulation studies on straight-line and elliptical paths further illustrate the merits of the variable L_0 guidance strategy.

This paper is organized as follows. Section 2 discusses the problem formulation. The proposed varying L_0 guidance law is presented in Section 3. Section 4 discusses simulation results, and Section 5 provides the concluding remarks.

2. PROBLEM FORMULATION

Consider a path-following scenario as illustrated in Fig. 1. Let the UAV state be $(x, y) \in \mathbb{R}^2$ with heading angle $\psi \in (-\pi, \pi]$ and constant speed $V_u > 0$. The objective here is to develop a prospective virtual target-based guidance law that governs the UAV heading angle while pursuing a virtual target T placed ahead along the path, eventually leading the UAV onto the desired path.

The kinematic equations of motion are described by

$$\dot{x} = V_u \cos \psi, \quad \dot{y} = V_u \sin \psi, \quad \dot{\psi} = \frac{a_d}{V_u}. \quad (1)$$

Here, a_d is the commanded lateral acceleration, whose upper bound is expressed as

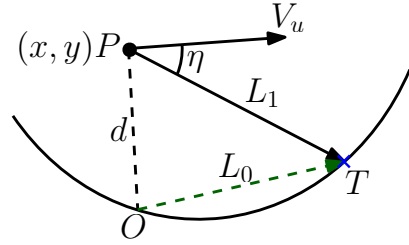


Fig. 2. Schematic of L_0 guidance logic.

$$a_d \in \left[-\frac{V_u^2}{R_{\min}}, \frac{V_u^2}{R_{\min}} \right]. \quad (2)$$

The curvature $\kappa = 1/R_{\min}$ ($R_{\min} > 0$ is minimum turn radius) is related to the a_d and is saturated as

$$\kappa = \frac{a_d}{V_u^2} \in \left[-\frac{1}{R_{\min}}, \frac{1}{R_{\min}} \right]. \quad (3)$$

Furthermore, path-following characteristics of the guidance method are evaluated using three performance indices, which are as follows:

$$\begin{aligned} \text{Settling time } t_s &= \inf\{t \geq 0 : |d(t)| \leq \varepsilon\} \text{ in s,} \\ \text{Control effort } J &= \int_0^{t_f} a_d^2(t) dt \text{ in } [\text{m}^2/\text{s}^3], \\ \text{Peak overshoot } M_{p\varepsilon} &= \max_{t \geq t_\varepsilon} (-d(t) - \varepsilon)^+, \end{aligned} \quad (4)$$

$$x^+ = \max\{x, 0\}.$$

Here, *peak overshoot* is the amount by which the trajectory goes above/below the lower band ε after the first entry, and t_f is a prescribed evaluation horizon.

3. VARYING L_0 GUIDANCE LOGIC

In this section, we briefly discuss the existing framework of L_0/L_1 guidance logic, followed by geometrical and theoretical discussion on the proposed variable L_0 guidance logic.

3.1 Background

Given the vehicle's position $P(x, y)$ defined in an inertial frame, a typical schematic of L_0 guidance logic is depicted in Fig. 2. Therein, we determine the closest point on the path to the vehicle as O , and the corresponding cross-track error as d . From that point, we advance a previously defined distance L_0 towards a virtual target T . The vector joining the current position of the vehicle and the reference point T is defined as the LOS vector, and the angle between L_1 and the vehicle's velocity V_u is defined as the heading error η , which is obtained as

$$\eta = \sin^{-1} \left(\frac{V_u \times L_1}{|V_u| |L_1|} \right). \quad (5)$$

Following the guidance logic used in Fernandes and Fontes (2024), L_1 relates to the tuning parameter L_0 (constant) and the local path curvature κ at the closest point O as

$$L_1 = \sqrt{d^2 + L_0^2(1 + d\kappa)} \equiv L_1(d, \kappa), \quad L_1 < 2R. \quad (6)$$

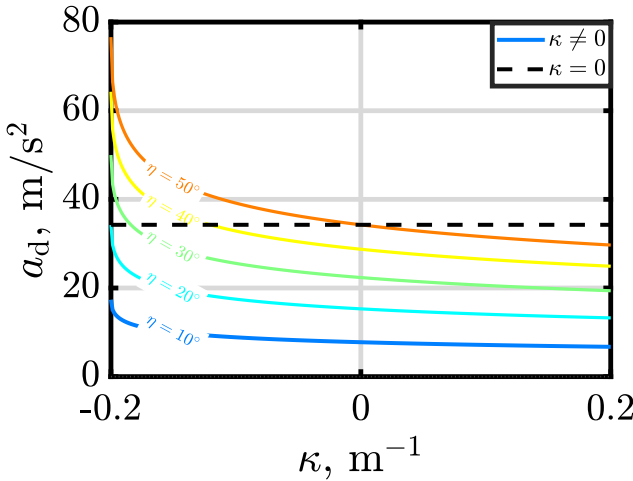


Fig. 3. Constant L_0 guidance with $(L_0, d) = (100, 50)$ m
For straight-line path, $\kappa = 0$ and therefore Eq.(6) simplifies to

$$L_1(d, \kappa) = \sqrt{d^2 + L_0^2} \quad (7)$$

For further details, please see Fernandes and Fontes (2024). While following the prescribed path, the centripetal acceleration required to follow an instantaneous circular arc formed by joining the UAV position and virtual target T on the path is expressed as

$$a_d = \frac{2V_u^2 \sin(\eta)}{L_1(d, \kappa)} = \frac{2V_u^2 \sin(\eta)}{\sqrt{d^2 + L_0(d)^2(1 + d\kappa)}} \quad (8)$$

However, one must consider the vehicle's dynamic capability, which ultimately limits heading angle variations. In this regard, define the saturation boundary by constraining η as

$$\bar{\eta}(d) = \arcsin\left(\min\{1, L_1(d, \kappa)/(2R_{\min})\}\right) \in (0, \pi/2) \quad (9)$$

Set three regions as

$$\begin{cases} S_1 = \{|\eta| \leq \bar{\eta}(d)\} & \text{(unsaturated)} \\ S_2 = \{\eta > \bar{\eta}(d)\}, & \\ S_3 = \{\eta < -\bar{\eta}(d)\} & \text{(saturated)} \end{cases} \quad (10)$$

Accordingly, the guidance command for the respective regions are expressed as

$$a_d = \begin{cases} \frac{2V_u^2}{L_1(d, \kappa)} \sin \eta & \text{if } (d, \eta) \in S_1, \\ \frac{2V_u^2}{L_1(d, \kappa)} \sin \bar{\eta} \text{ sign}(\bar{\eta}) & \text{if } (d, \eta) \in S_2, S_3 \end{cases} \quad (11)$$

In practice, estimating the virtual target on the path from onboard measurements and implementing the corresponding guidance commands inevitably introduces a projection error. A practical way to mitigate this is to constrain that error within a prescribed bound. To this end, we work in the local Frenet frame at the closest path point O , project the virtual target T along the tangent at O as T' , and explicitly quantify the resulting projection error TT' , which then guides the control design. On this geometric basis, we develop the variable L_0 guidance law, its construction and properties in the subsequent section.

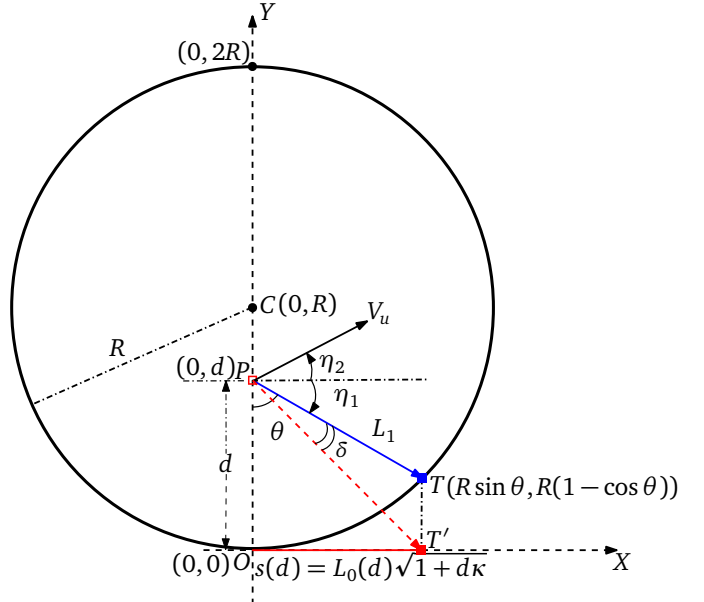


Fig. 4. L_0 feasibility study

3.2 Feasibility set and geometric bounds

Consider $O \in \mathbb{R}^2$ be the closest point on the path, with tangent OX and inward normal OY as shown in Fig. 4. Let the vehicle be at $P = (0, d)$ and denote the local curvature at O by κ (radius $R = 1/|\kappa|$). We place a virtual target on the path ahead of O by choosing a length s along the tangent,

$$s(d, \kappa) := L_0(d) \sqrt{1 + d\kappa}, \quad 1 + d\kappa > 0, \quad (12)$$

Thus, LOS vector is $L_1 = T' - P = (s, -d)$ and magnitude is computed as

$$L_1(d, \kappa) = \|T' - P\| = \sqrt{d^2 + L_0^2(d)(1 + d\kappa)}. \quad (13)$$

Accordingly, the projection error δ can be obtained as

$$\begin{aligned} \|\delta\| &= \|T - T'\| = \|(R \sin \theta - s, R(1 - \cos \theta))\| \\ &\leq \frac{|\kappa| s^2}{2} + O((\kappa s)^4) \end{aligned} \quad (14)$$

To guarantee $\|\delta\| \leq \varepsilon_{\text{proj}}$, one may use

$$s \leq \sqrt{\frac{2\varepsilon_{\text{proj}}}{|\kappa|}} \quad (\kappa \neq 0). \quad (15)$$

A practical consideration for design is given as

$$s = \min\left\{L_0 \sqrt{1 + d\kappa}, \sqrt{\frac{2\varepsilon_{\text{proj}}}{|\kappa|}}\right\} \quad (16)$$

In this context, one can define the feasibility set while ensuring the virtual target lies ahead of the vehicle along the instantaneous circular arc.

Definition 1. For any circular arc of radius R and curvature $\kappa(s^*)$ at the closest point O , define a feasibility set

$$\begin{aligned} \mathcal{F} := \left\{ (d, \eta) \in \mathbb{R} \times (-\pi, \pi] : 1 + d\kappa(s^*) > 0, \right. \\ \left. L_1(d, \kappa) \leq 2R - d \right\}. \end{aligned} \quad (17)$$

with $R = 1/|\kappa(s^*)|$ (and $R = \infty$ if $\kappa = 0$), and

$$\begin{aligned} L_1(d, \kappa) &= \sqrt{d^2 + L_0^2(1 + d\kappa(s^*))}, \\ s &= L_0 \sqrt{1 + d\kappa(s^*)}. \end{aligned} \quad (18)$$

Though the commanded lateral acceleration (unsaturated) is given by Eq. (8), the local path curvature sensitivity with a_d is explained subsequently.

3.3 Curvature sensitivity of a_d

For fixed (V_u, η) , using Eq. (8)

$$\begin{aligned} \frac{\partial a_d}{\partial \kappa} \Big|_{\eta} &= -\frac{2V_u^2 \sin \eta}{L_1^2} \frac{\partial L_1}{\partial \kappa} = -\frac{2V_u^2 \sin \eta}{L_1^2} \cdot \frac{L_0^2(d) d}{2L_1} \\ &= -\frac{V_u^2 \sin \eta L_0^2(d) d}{(d^2 + L_0^2(d)(1 + d\kappa))^{3/2}}. \end{aligned} \quad (19)$$

A dimensionless curvature sensitivity index (CSI) σ is defined as

$$\sigma = \frac{\kappa}{a_d} \frac{\partial a_d}{\partial \kappa} \Big|_{\eta} = -\frac{\kappa L_0^2(d) d}{2(d^2 + L_0^2(d)(1 + d\kappa))} \quad (20)$$

Two useful limits are stated as follows:

(1) *Small $d\kappa$ (first order, no d/L_0 assumption):*

$$\sigma \approx -\frac{\kappa L_0^2(d) d}{2(d^2 + L_0^2(d))} \quad (21)$$

If in addition $|d| \ll L_0(d)$ (near-path), then

$$\sigma \approx -\frac{\kappa d}{2} \quad (22)$$

(2) *Large L_0 (far field):*

$$\sigma \approx -\frac{\kappa d}{2(1 + d\kappa)}, \quad |\sigma| < \frac{1}{2} \quad (23)$$

Thus Eq. (8) is curvature-sensitive, but the sensitivity is attenuated by increasing $L_0(d)$ far from the path. For near-path linearization (small $|\eta|$), using $\sin \eta \simeq \eta = \frac{d}{L_1}$ and the standard small-angle L_1 -geometry relation yields,

$$a_d \approx \frac{2V_u^2 \eta}{L_1} \approx \frac{2V_u^2 d}{L_1^2} = \frac{2V_u^2 d}{d^2 + L_0^2(d)(1 + d\kappa)}. \quad (24)$$

Thus using Eq. (24),

$$\frac{\partial a_d}{\partial \kappa} \approx -\frac{2V_u^2 d^2 L_0^2(d)}{(d^2 + L_0^2(d)(1 + d\kappa))^2} \quad (25)$$

which is always negative for $d \neq 0$, and increasing κ reduces a_d . Fig. 3 illustrates that the variation in a_d is prominent with an increase in $|\kappa|$ while varying η .

3.4 Guidance law

In contrast to the constant L_0 , we propose a varying L_0 profile denoted as $L_0^v(d)$, which is expressed as

$$L_0^v(d) = L_{\min} + (L_{\max} - L_{\min}) \left(1 - e^{-|d|/d_c}\right) \quad (26)$$

with parameters $L_{\max} > L_{\min} > 0$, $d_c > 0$. Table 1 illustrate the effect of design parameter (L_{\max}, d_c) on the $L_0^v(d)$ and the resulting a_d . For a fair comparative analysis between the two guidance methods, we use constant L_0 denoted as $L_0^c(d)$ as

$$L_0^c(d) \equiv L_{\min} \quad (27)$$

The corresponding LOS lengths of the two guidance laws using Eq. (6) are expressed as

$$L_1^c(d, \kappa) = \sqrt{d^2 + L_{\min}^2(1 + d\kappa)}, \quad (28)$$

$$L_1^v(d, \kappa) = \sqrt{d^2 + L_0^v(d)(1 + d\kappa)}. \quad (29)$$

If $L_0^v(d) \in [L_{\min}, L_{\max}]$, with $L_{\min} > 0$ and $L_0^v(d)$ is non decreasing in $|d|$ then,

$$\sqrt{d^2 + L_{\min}^2(1 + d\kappa)} \leq L_1^v(d, \kappa) \leq \sqrt{d^2 + L_{\max}^2(1 + d\kappa)}. \quad (30)$$

Lemma 1. (Monotone envelope). For all feasible (d, κ) with $1 + d\kappa > 0$,

$$L_1^v(d, \kappa) \geq L_1^c(d, \kappa). \quad (31)$$

Proof. Since mapping of $x \mapsto \sqrt{d^2 + x^2(1 + d\kappa)}$ is increasing when $1 + d\kappa > 0$ and $L_0^v(d) \geq L_{\min}$, hence leads to (31). \square

Lemma 2. (Quantitative difference). Subject to Lemma 1 and LOS lengths $L_1^c(d, \kappa)$, $L_1^v(d, \kappa)$ given by Eq.(28) and (29), respectively then for each fixed (d, κ)

$$\begin{aligned} \Delta L_1(d, \kappa) &= L_1^v(d, \kappa) - L_1^c(d, \kappa) \\ &= \frac{L_0^v(d) - L_{\min}^2}{L_1^v(d, \kappa) + L_1^c(d, \kappa)} (1 + d\kappa) \geq 0 \end{aligned} \quad (32)$$

Thus, using Eq. (9), the difference in saturation region of heading error is deduced as

$$\Delta \bar{\eta}(d) = \bar{\eta}^v(d) - \bar{\eta}^c(d) \geq \frac{\Delta L_1}{2R_{\min} \sqrt{1 - (L_1^v/(2R_{\min}))^2}}. \quad (33)$$

Moreover, in the far field $|d| \gg d_c$ where $L_0^v(d) \approx L_{\max}$,

$$\Delta \bar{\eta} \approx \arcsin \frac{L_{\max}}{2R_{\min}} - \arcsin \frac{L_{\min}}{2R_{\min}}, \quad (34)$$

and the time difference is

$$\Delta T_{\text{far}} \approx -\frac{R_{\min}}{V_u} \Delta \bar{\eta}. \quad (35)$$

Proof. From the fact that $(L_1^v(d, \kappa))^2 - L_1^c(d, \kappa)^2 = (L_0^v(d, \kappa) - L_{\min}^2)(1 + d\kappa)$ with the factorization reduces to Eq. (32) as $L_1^v(d, \kappa) - L_1^c(d, \kappa) = \frac{(L_1^v(d, \kappa))^2 - (L_1^c(d, \kappa))^2}{L_1^v(d, \kappa) + L_1^c(d, \kappa)}$. Next, using $\bar{\eta} = \arcsin(L_1/(2R_{\min}))$ on the unsaturated branch and hence, $\frac{d}{dL_1} \arcsin(L_1/(2R_{\min})) = \frac{1}{2R_{\min} \sqrt{1 - (L_1/(2R_{\min}))^2}}$. Consequently, evaluating at $L_1(d, \kappa) = L_1^v(d, \kappa)$ and applying the mean-value inequality yields the bound (33). Finally, when $|d| \gg d_c$ we have $L_0^v(d, \kappa) \approx L_{\max}$, giving (34) and the time reduction in saturation from $|\dot{\eta}| \geq V_u/R_{\min}$. \square

The theoretical analysis discussed above is simulated with parameters $(V_u, g, L_{\min}, L_{\max}, d_c) = (50 \text{ m/s}, 9.8 \text{ m/s}^2, 50 \text{ m}, 150 \text{ m}, 30 \text{ m})$ for $R_{\min} = 100 \text{ m}$, $\eta \in (-\pi, \pi]$ rad, and $d \in [0, 200] \text{ m}$. The saturation boundary $\bar{\eta}$ follow Eq. (9), wherein, $L_1(d, \kappa)$ will be substituted by Eq. (28) and (29) for the two guidance laws. The corresponding saturation regions satisfy Eq. (10). To quantify the improvement contributed by the variable $L_0(d)$ profile over the constant L_0 guidance law, we define two complementary metrics based on the unsaturated region area in the (d, η) plane. Let $\mathcal{A}_{\text{const}}$ denote the fraction of the (d, η) plane where the constant L_0 guidance law remains unsaturated, and \mathcal{A}_{var} denote the corresponding fraction for the variable $L_0(d)$ profile. These are computed as:

$$\mathcal{A}_{\text{const}} = \frac{1}{N} \sum_{i=1}^N \mathbb{1}(|\eta_i| < \bar{\eta}_{\text{const}}(d_i)), \quad (36)$$

$$\mathcal{A}_{\text{var}} = \frac{1}{N} \sum_{i=1}^N \mathbb{1}(|\eta_i| < \bar{\eta}_{\text{var}}(d_i)) \quad (37)$$

where N is the total number of grid points, $\mathbb{1}(\cdot)$ is the indicator function, and $\bar{\eta}(d)$ represents the saturation boundary in heading error.

Absolute Gain (percentage points): This metric measures the direct increase in the unsaturated region as a difference in percentage points described by

$$G_{\text{abs}} = (\mathcal{A}_{\text{var}} - \mathcal{A}_{\text{const}}) \times 100\%. \quad (38)$$

The absolute gain provides an intuitive measure of how many additional percentage points of the (d, η) plane remain unsaturated when using the variable $L_0(d)$ strategy.

Relative Gain (percentage increase): This metric quantifies the proportional improvement relative to the baseline derived as

$$G_{\text{rel}} = \left(\frac{\mathcal{A}_{\text{var}}}{\mathcal{A}_{\text{const}}} - 1 \right) \times 100\%. \quad (39)$$

The relative gain expresses how much larger the unsaturated region becomes as a percentage of the original constant L_0 baseline, providing a normalized measure of effectiveness. Fig. 5 illustrates the relative comparison of operational envelope. Fig. 5a and 5b correspond to operational regions for constant L_0 and variable L_0 guidance laws, respectively. At the ratio $L_{\text{max}}/L_{\text{min}} = 3.0$ (corresponding to $L_{\text{max}} = 150$ m for $L_{\text{min}} = 50$ m), the variable lookahead strategy achieves $\mathcal{A}_{\text{abs}} = 17.32\%$ and $\mathcal{A}_{\text{rel}} = 72.58\%$, demonstrating that the unsaturated region expands from 23.86% to 41.17% of the (d, η) plane as gain region indicated in green in Fig. 5c. Furthermore, a detailed analysis of the ratio $\in [1, 5]$ is shown in Fig. 5d. The absolute gain (green, left axis) shows the direct benefit in percentage points, while the relative gain (magenta, right axis) demonstrates the proportional enhancement. Both metrics increase with the ratio, with marginal benefits observed at higher values, suggesting an optimal design range for practical implementation.

Corollary 1. With $\bar{\eta}^c(d), \bar{\eta}^v(d)$ computed from $L_1^c(d, \kappa)$, $L_1^v(d, \kappa)$, from Eq.(28) and (29),

$$\bar{\eta}^v(d) \geq \bar{\eta}^c(d) \Rightarrow S_1^v \supseteq S_1^c. \quad (40)$$

Figure 6 illustrates the polar-like representation of comparative study, where each point in the circular plot corresponds to a state (d, η) represented in Cartesian coordinates as $(d \cos \eta, d \sin \eta)$. The concentric dashed circles indicate constant cross-track error levels ($d = 50$ m and $d = 100$ m), while the outer solid circle marks the boundary at $d = 150$ m.

Figure 6a illustrates that the unsaturated region S_1^c (light green) forms a relatively narrow band around the horizontal axis ($\eta \approx 0$). The saturation boundary $\bar{\eta}(d)$ (solid black curves) defines the transition between the unsaturated region and the saturated regions S_2^c (light red, $\eta > \bar{\eta}$) and S_3^c (light blue, $\eta < -\bar{\eta}$). In Figure 6b, the unsaturated region S_1^v (light green) expands significantly compared to Figure 6a, as discussed previously and analyzed in detail in Figure 5. The circular representation clearly illustrates the geometric advantage of the variable L_0 strategy: the

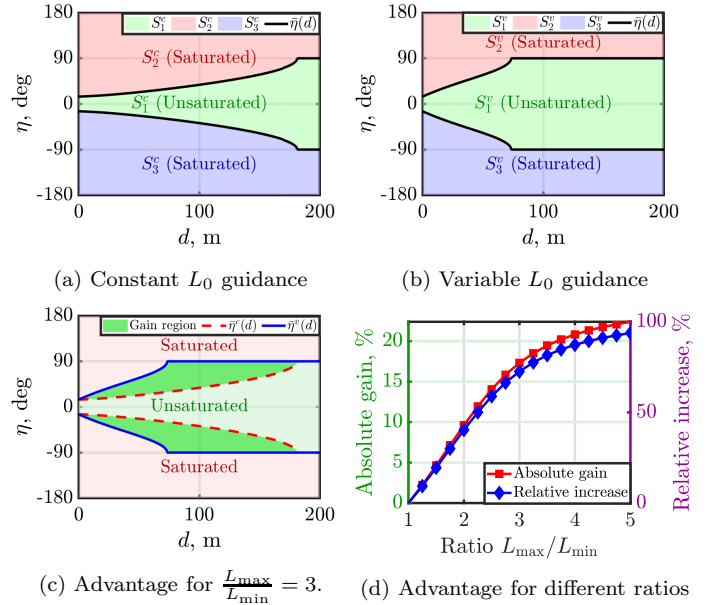


Fig. 5. Enlarged envelope analysis of two guidance laws

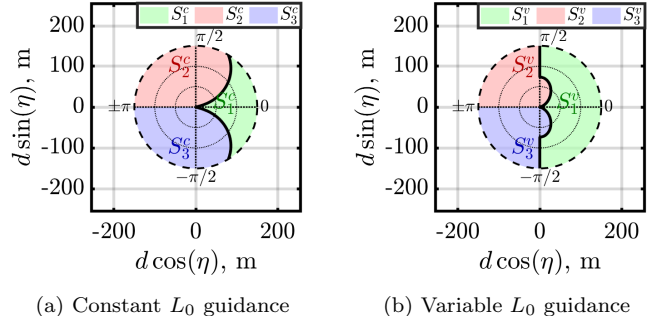


Fig. 6. Polar like representation of $\eta - d$ space for $\frac{L_{\text{max}}}{L_{\text{min}}} = 3$.

unsaturated region S_1^v strictly contains S_1^c (i.e., $S_1^v \supseteq S_1^c$), confirming Corollary 2. The added region $S_1^v \setminus S_1^c$ represents states for which the variable L_0 formulation remains unsaturated even though the constant L_0 baseline would saturate.

Lemma 3. (Saturated exit time bound). From any initial $(d(0), \eta(0))$,

$$T_{\text{far}}(L_0) \leq \frac{R_{\text{min}}}{V_u} (|\eta(0)| - \bar{\eta}(d(0)))^+. \quad (41)$$

Hence $T_{\text{far}}^{\text{v,u}} \leq T_{\text{far}}^c$. Further,

$$\int_0^{T_{\text{far}}} a^2 dt \leq (V_u^2/R_{\text{min}})^2 T_{\text{far}},$$

so the saturated-phase control effort is no greater for the variable profile.

Proof. In saturation $|a| = V^2/R_{\text{min}}$ and $|\dot{\eta}| \geq V/R_{\text{min}}$. The angle distance to the boundary is reduced when $\bar{\eta}(d)$ is larger, which holds by Corollary 1. \square

Lemma 4. (Near-path linear rate). In S_1 both laws share the same local time constant

$$\tau = \frac{L_{\text{min}}}{V}, \quad (42)$$

since $L_0^v(0) = L_{\text{min}}$ and $L_1 \rightarrow L_{\text{min}}$ near the path.

Table 1. Combined effect of L_{\max} and d_c on variable L_0 guidance law performance

Parameter	Effect on L_0	Effect on a_d	Characteristics	Remarks
Higher L_{\max}	Larger L_0 at large d	Lower acceleration	Slower, smoother	Stable flight
Lower L_{\max}	Smaller L_0 at large d	Higher acceleration	Faster, aggressive	Performance priority
Lower d_c	Faster saturation	Lower at medium d	Slower from medium d	Minimize oscillations
Higher d_c	Slower saturation	Higher at medium d	Faster from medium d	Fast initial convergence

3.5 Stability properties

Lemma 5. Let

$$L_1^2(d, \kappa) = d^2 + L_0(d)^2(1 + d\kappa) \quad (43)$$

with $L_0 : \mathbb{R} \rightarrow \mathbb{R}_+$ of class C^1 . Then

$$\frac{\partial}{\partial d}(L_1^2(d, \kappa)) = 2 \left[d + (1 + d\kappa)L_0(d)L_0'(d) + \frac{1}{2}\kappa L_0(d)^2 \right] \quad (44)$$

In particular, defining

$$g(d) = d + (1 + d\kappa)L_0(d)L_0'(d) + \frac{1}{2}\kappa L_0(d)^2. \quad (45)$$

we have $\frac{\partial}{\partial d}(L_1^2) = 2g(d)$

Proof. Differentiate $L_1^2(d, \kappa) = d^2 + L_0(d)^2(1 + d\kappa)$ using the product rule leads to

$$\begin{aligned} \frac{\partial}{\partial d}(L_1^2) &= 2d + 2L_0L_0'(1 + d\kappa) + L_0^2\kappa \\ &= 2 \left[d + (1 + d\kappa)L_0L_0' + \frac{1}{2}\kappa L_0^2 \right] \end{aligned} \quad (46)$$

□

Lemma 6. Suppose $L_0(\cdot)$ is even and nondecreasing in $|d|$, and the feasibility condition $1 + d\kappa > 0$ holds (e.g., on the standard feasible set). Then $g(d)$ has the same sign as d , and for

$$\Phi(d) := \int_0^d \frac{g(\xi)}{L_1(\xi, \kappa)^2} d\xi \quad (47)$$

we have $\Phi(d) \geq 0$ with equality iff $d = 0$.

Proof. By Lemma 5, $2g(d) = \partial_d L_1^2(d, \kappa)$. With L_0 even and nondecreasing in $|d|$ and $1 + d\kappa > 0$, the map $d \mapsto L_1^2(d, \kappa)$ is strictly increasing for $d > 0$ and strictly decreasing for $d < 0$, hence $g(d)$ has the sign of d . Since $L_1^2 > 0$, the integrand $\frac{g(\xi)}{L_1(\xi, \kappa)^2}$ has the sign of ξ , so the integral from 0 to d is nonnegative and only vanishes at $d = 0$. □

Lemma 7. With $g(d)$ as in Lemma 5 and the geometry above, the following identity holds:

$$\frac{g(d)}{L_1(d, \kappa)} = \sin \eta_1 \cos \eta_2 + \cos \eta_1 \sin \eta_2 - \sin \eta_2 \cos(\eta_1 + \eta_2). \quad (48)$$

Proof. Use the identities $\sin(\eta_1 + \eta_2) = \sin \eta_1 \cos \eta_2 + \cos \eta_1 \sin \eta_2$ and $\cos(\eta_1 + \eta_2) = \cos \eta_1 \cos \eta_2 - \sin \eta_1 \sin \eta_2$. A direct substitution of $\sin \eta_1 = d/L_1$ and $\cos \eta_1 = L_0\sqrt{1+d\kappa}/L_1$ into the right-hand side followed by collecting terms yields

$$\begin{aligned} \sin \eta_1 \cos \eta_2 + \cos \eta_1 \sin \eta_2 - \sin \eta_2 \cos(\eta_1 + \eta_2) \\ = \frac{1}{L_1} \left[d + (1 + d\kappa)L_0L_0' + \frac{1}{2}\kappa L_0^2 \right] \end{aligned} \quad (49)$$

where the bracket equals $g(d)$ by Lemma 5. □

Theorem 1. Consider a vehicle moving with a constant speed $V_u > 0$ near a regular C^2 path and the reduced Frenet error dynamics described by

$$\begin{aligned} \dot{d} &= -V_u \sin \eta_2, & \dot{\eta}_2 &= \frac{a_d}{V_u}, \\ \dot{\eta}_1 &= -\frac{V_u}{L_1} \sin(\eta_2 - \eta_1), \\ \dot{\eta} &= \frac{a_d}{V_u} + \frac{V_u}{L_1} \sin \eta. \end{aligned} \quad (50)$$

For every initial $(d(0), \eta(0)) \in \mathcal{F}$, the solution is forward complete using heading guidance Eq. (11), and hence

$$(d(t), \eta(t)) \rightarrow (0, 0) \quad \text{as } t \rightarrow \infty. \quad (51)$$

Proof. We present three cases that correspond to the regions $S_2 \cup S_3$, the boundary $|\eta| = \bar{\eta}(d)$, and the unsaturated region S_1 .

Case 1 (Saturated \rightarrow Unsaturated in finite time): While $(d, \eta) \in S_2 \cup S_3$, the applied acceleration has constant magnitude $|a| = V_u^2/R_{\min}$. Hence, from (50),

$$\begin{aligned} |\dot{\eta}| &= \left| \frac{a_d}{V_u} + \frac{V_u}{L_1} \sin \eta \right| \geq \frac{V_u}{R_{\min}} - \frac{V_u}{L_1} \sin \bar{\eta} \\ &= \frac{V_u}{R_{\min}} - \frac{V_u}{L_1} \frac{L_1}{2R_{\min}} = \frac{V_u}{2R_{\min}}. \end{aligned} \quad (52)$$

Therefore the angular distance from $|\eta(0)|$ to $\bar{\eta}(d(0))$ is covered in finite time given by Eq. (41). Thus every trajectory starting in $S_2 \cup S_3$ enters S_1 in finite time.

Case 2 (Invariance of S_1): On $|\eta| = \bar{\eta}(d)$, using the saturated law,

$$\dot{\eta} = \frac{2V_u}{L_1} \sin \bar{\eta} \operatorname{sgn}(\eta) + \frac{V_u}{L_1} \sin \eta = \frac{V_u}{L_1} (\sin \bar{\eta} \operatorname{sgn}(\eta) + \sin \eta) \quad (53)$$

which is zero at $\eta = \pm \bar{\eta}$ and points toward the interior for small excursions beyond the boundary. Hence S_1 is positively invariant.

Case 3 (Lyapunov analysis in S_1): Inside S_1 the guidance law satisfy $a_d = \frac{2V_u^2}{L_1} \sin \eta$. Define the Lyapunov function as

$$\mathcal{V}(d, \eta) = \frac{1}{2}V_u^2 \sin^2 \eta + V_u^2 \Phi(d), \quad (54)$$

which is positive definite on \mathcal{F} with unique minimum at $(d, \eta) = (0, 0)$. Differentiate \mathcal{V} in Eq.(54) along Eq.(50) and on simplifying using Lemma 5-7 results in

$$\dot{\mathcal{V}} = -\frac{2V_u^3}{L_1(d, \kappa)} \sin^2 \eta_2 \cos \eta_1 \leq 0. \quad (55)$$

In the feasible set, $s \geq 0$ so $\cos \eta_1 = s/L_1(d, \kappa) \geq 0$, equality holds only at $\sin \eta = 0$. Hence, \mathcal{V} is nonincreasing in S_1 . By LaSalle's invariance principle, the ω -limit set is contained in $\{\sin \eta = 0\} \cap S_1$, i.e., $\eta = 0$. On $\eta = 0$ we have $\dot{d} = 0$ and $\dot{\mathcal{V}} = 0$, which implies $g(d) = 0$. Since

$g(d)$ has the sign of d , this implies $d = 0$. Thus, the only invariant set with $\dot{\mathcal{V}} = 0$ is $(d, \eta) = (0, 0)$, and hence the equilibrium is asymptotically stable. Combining Steps A–C yields forward completeness and $(d(t), \eta(t)) \rightarrow (0, 0)$ for all initial conditions in \mathcal{F} . \square

4. SIMULATION RESULTS

This section discusses numerical simulation studies for constant L_0 and varying L_0 guidance methods, while following straight-line and elliptic paths. In doing so, three performance indices, such as settling time, the control effort, and peak overshoot, are analyzed with variation in tunable parameters (L_{\min}, L_{\max}, d_c) over a total run time t_f . Unless stated, the speed of the UAV is considered as $V_u = 12$ m/s. Simulation parameters for constant $L_0 = L_{\min}$ and the variable L_0 as governed by Eq. (26), are listed in Table 2.

Table 2. Simulation parameters

Case study	Initial conditions (x_0, y_0) m, ψ_0 deg	Constant L_0 $L_0 = L_{\min}$ m	Variable L_0 (L_{\max}, d_c) m
Straight line	(−150, 50), 90	40	82, 32
Elliptic path	(250, 120), 150	22	100, 20

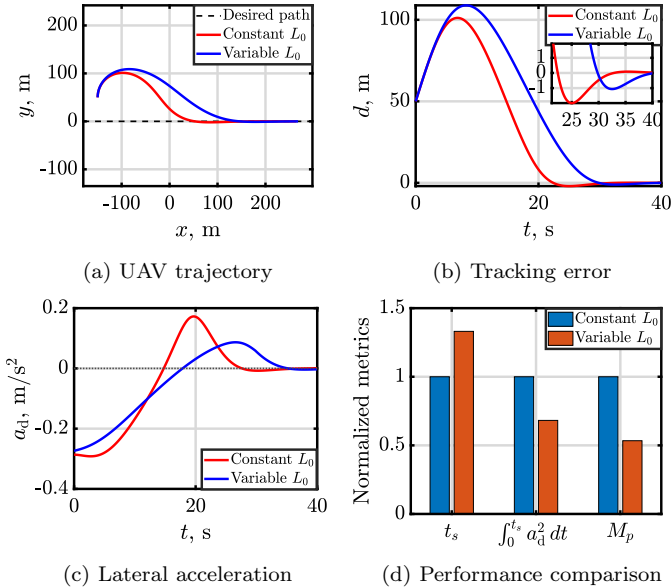


Fig. 7. Results for straight line following

In the case study of straight line path following, the desired path is described by $y = 0$. The numerical simulation results are shown in Fig. 7. Fig. 7a plots the UAV trajectory, and the corresponding tracking error is plotted in Fig. 7b. While both methods reduce the tracking error to zero and eventually align with the desired line, the variable L_0 approach exhibits significantly smaller overshoot in comparison to constant L_0 as indicated in Fig. 7b. The commanded lateral acceleration is depicted in Fig. 7c. It is noteworthy to highlight that, the lateral acceleration profile demonstrates a substantial reduction in control effort, as reflected in both the lower peak acceleration as in Fig. 7c and the reduced integrated squared acceleration metric indicated in Fig. 7d.

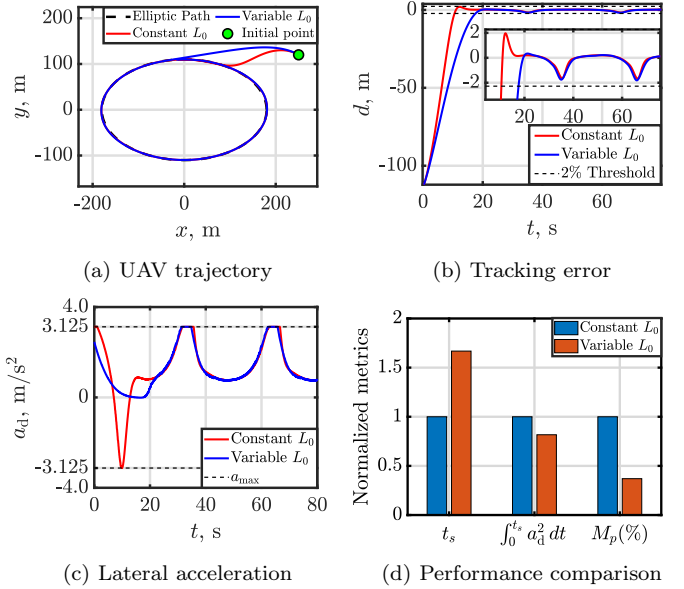


Fig. 8. Results for elliptic path following

For an elliptic path following case study, the desired path is characterized by $\frac{x^2}{180^2} + \frac{y^2}{110^2} = 1$. Simulation results are illustrated in Fig. 8. Fig. 8a shows the UAV trajectory, and the tracking error profile is depicted in Fig. 8b. As seen in Fig. 8b, the variable L_0 guidance reduces the tracking error to negligibly low value and exhibits significantly smaller overshoot. This improvement is achieved while maintaining a smoother lateral acceleration profile, as shown in Fig. 8c, where the constant L_0 case produces larger and more frequent acceleration peaks due to its inability to adapt the look-ahead distance. The performance metrics in Fig. 8d establish that the variable L_0 guidance yields reduced control effort and overshoot, demonstrating that adaptively increasing the look-ahead distance for large initial deviations effectively prevents saturation and improves transient response.

5. CONCLUSIONS

This work presents an adaptive look-ahead guidance strategy that enhances UAV path-following performance by exploiting the geometric relationship between tracking errors and the look-ahead distance. By characterizing the saturated and unsaturated regions in the (d, η) error space, the proposed variable L_0 method expands the unsaturated operating envelope compared with the constant L_0 baseline. A key contribution of this study is the ratio analysis of L_{\max}/L_{\min} , which quantifies how the envelope expands as this ratio increases. The results show that for ratios greater than 3, the unsaturated region grows by more than 70%, enabling the guidance law to remain unsaturated over a significantly broader range of tracking errors. This enlarged operational region directly contributes to smoother trajectory corrections, earlier exit from saturation, and reduced overall control effort. Simulation studies on straight-line and elliptic paths confirm that dynamically adjusting the look-ahead distance yields smooth converging behaviour, reduced overshoot, and a substantial reduction in control effort. These improvements demonstrate the practical significance of incorporating adaptive look-ahead mechanisms into UAV guidance design, offering a compu-

tationally efficient approach that enhances maneuvering efficiency and robustness under realistic actuator and curvature constraints paths. These insights also open research directions for extending variable-parameter guidance laws to more complex path geometries and higher-order vehicle models.

REFERENCES

Alessandretti, A., Aguiar, A.P., and Jones, C.N. (2013). Trajectory-tracking and path-following controllers for constrained underactuated vehicles using model predictive control. In *2013 European Control Conference (ECC)*, 1371–1376. doi:10.23919/ECC.2013.6669717.

Breivik, M. and Fossen, T.I. (2005). Principles of guidance-based path following in 2d and 3d. In *Proceedings of the 44th IEEE Conference on Decision and Control*, 627–634. IEEE.

Curry, R., Lizarraga, M., Mairs, B., and Elkaim, G.H. (2013). l_2^+ , an improved line of sight guidance law for uavs. In *2013 American Control Conference*, 1–6. IEEE.

Fernandes, M.C.R.M. and Fontes, F.A.C.C. (2024). A path-following guidance method for nonholonomic vehicles with a large domain of attraction for straight and curved paths. In *2024 European Control Conference (ECC)*, 621–626. doi:10.23919/ECC64448.2024.10590773.

Fernandes, M.C.R.M., Paiva, L.T., and Fontes, F.A.C.C. (2020). A model predictive control scheme to improve performance of a path-following controller for airborne wind energy. Berlin.

Fernandes, M.C.R.M., Vinha, S., Paiva, L.T., and Fontes, F.A.C.C. (2022). L0 and L1 guidance and path-following control for airborne wind energy systems. *Energies*, 15(4). doi:10.3390/en15041390. URL <https://www.mdpi.com/1996-1073/15/4/1390>.

Fernandes, M.C., Shivam, A., Fagiano, L., and Fontes, F.A. (2025). Varying l0 path-following guidance for airborne wind energy systems. *IFAC-PapersOnLine*, 59(16), 128–133. doi: <https://doi.org/10.1016/j.ifacol.2025.10.091>. 11th IFAC Symposium on Robust Control Design ROCOND 2025.

Frew, E.W., Lawrence, D.A., and Morris, S. (2008). Co-ordinated Standoff Tracking of Moving Targets Using Lyapunov Guidance Vector Fields. *Journal of Guidance, Control, and Dynamics*, 31(2), 290–306. doi:10.2514/1.30507.

Goncalves, V.M., Pimenta, L.C., Maia, C.A., and Pereira, G.A. (2009). Artificial Vector Fields for Robot Convergence and Circulation of Time-Varying Curves in n-Dimensional Spaces. In *Proceedings IEEE American Control Conference*, June, 2012–2017. doi:10.1109/ACC.2009.5160350.

Hota, S. and Ghose, D. (2014). Curvature-constrained trajectory generation for waypoint following for miniature air vehicle. *Proceedings of the Institution of Mechanical Engineers, Part G: Journal of Aerospace Engineering*, 228(11), 2066–2082.

Kapitanyuk, Y.A., de Marina, H.G., Proskurnikov, A.V., and Cao, M. (2017). Guiding Vector Field Algorithm for a Moving Path Following Problem. *IFAC-PapersOnLine*, 50(1), 6983–6988.

Kumar, S., Sinha, A., and Kumar, S.R. (2024). Robust path-following guidance for an autonomous vehicle in the presence of wind. *Aerospace Science and Technology*, 150, 109225. doi: <https://doi.org/10.1016/j.ast.2024.109225>.

Lee, S., Cho, A., and Kee, C. (2010). Integrated waypoint path generation and following of an unmanned aerial vehicle. *Aircraft Engineering and Aerospace Technology*, 82(5), 296–304.

Lekkas, A.M. and Fossen, T.I. (2012). A time-varying lookahead distance guidance law for path following. *IFAC Proceedings Volumes*, 45(27), 398–403.

Lekkas, A.M. and Fossen, T.I. (2014). Integral los path following for curved paths based on a monotone cubic hermite spline parametrization. *IEEE Transactions on Control Systems Technology*, 22(6), 2287–2301.

Nelson, D.R., Barber, D.B., McLain, T.W., and Beard, R.W. (2007). Vector field path following for miniature air vehicles. *IEEE Transactions on Robotics*, 23(3), 519–529. doi:10.1109/TRO.2007.898976.

Osborne, J. and Rysdyk, R. (2005). Waypoint guidance for small uavs in wind. In *AIAA Guidance, Navigation, and Control Conference, AIAA Paper 2005-6951*, September. doi:10.2514/6.2005-6951.

Park, S., Deyst, J., and How, J. (2004). A New Nonlinear Guidance Logic for Trajectory Tracking. In *AIAA Guidance, Navigation, and Control Conference and Exhibit*. American Institute of Aeronautics and Astronautics. doi:DOI: 10.2514/6.2004-4900. URL <https://arc.aiaa.org/doi/abs/10.2514/6.2004-4900>.

Park, S., Deyst, J., and How, J. (2007). Performance and Lyapunov Stability of a Nonlinear Path Following Guidance Method. *Journal of Guidance, Control and Dynamics*, 30(6). doi:<https://doi.org/10.2514/1.28957>.

Pothen, A.A. and Ratnoo, A. (2017). Curvature-Constrained Lyapunov Vector Field for Standoff Target Tracking. *Journal of Guidance, Control, and Dynamics*, 40(10), 2729–2736. doi:10.2514/1.G002281.

Ratnoo, A., Hayoun, S.Y., Granot, A., and Shima, T. (2015). Path Following Using Trajectory Shaping Guidance. *Journal of Guidance, Control, and Dynamics*, 38(1), 106–116. doi:10.2514/1.G000300.

Shivam, A. and Ratnoo, A. (2021). Curvature-constrained vector field for path following guidance. In *2021 International Conference on Unmanned Aircraft Systems (ICUAS)*, 853–857. doi:10.1109/ICUAS51884.2021.9476741.

Shivam, A. and Ratnoo, A. (2023). Arcsine Vector Field for Path Following Guidance. *Journal of Guidance, Control, and Dynamics*, 46(12), 2409–2420. doi:10.2514/1.G007562.

Silva, G.B., Paiva, L.T., and Fontes, F.A. (2019). A path-following guidance method for airborne wind energy systems with large domain of attraction. In *2019 American Control Conference (ACC)*, 2771–2776. IEEE.

Stastny, T. (2018). L1 guidance logic extension for small uavs: handling high winds and small loiter radii. *arXiv preprint arXiv:1804.04209*.

Thakar, S. and Ratnoo, A. (2017). A Tangential Guidance Logic for Virtual Target Based Path Following. In *AIAA Guidance, Navigation, and Control Conference, AIAA Paper 2017-1042*, January. doi:10.2514/6.2017-1042.